Mechanistic Origin of the High Performance of Yolk@Shell Bi$_2$S$_3$@N-Doped Carbon Nanowire Electrodes

Longze Zhao,[†,#] Hong-Hui Wu,[‡,#] Chenghao Yang,[§] Qiaobao Zhang,[*,†] Guiming Zhong,[‖] Zhiming Zheng,[†] Huixin Chen,[‖] Jinming Wang,[†] Kai He,[○] Baolin Wang,[⊥] Ting Zhu,[⊥,∇] Xiao Cheng Zeng,[*,‡] Meilin Liu,[∇] and Ming-Sheng Wang[*,†]

[†]Department of Materials Science and Engineering, College of Materials, and Pen-Tung Sah Institute of Micro-Nano Science and Technology, Xiamen University, Xiamen, Fujian 361005, China

[‡]Department of Chemistry, University of Nebraska-Lincoln, Lincoln, Nebraska 68588, United States

[§]Guangzhou Key Laboratory for Surface Chemistry of Energy Materials, New Energy Research Institute, School of Environment and Energy, South China University of Technology, Guangzhou 510006, China

[‖]Xiamen Institute of Rare Earth Materials, Haixi Institutes, Chinese Academy of Sciences, Xiamen 361024, China

[⊥]Woodruff School of Mechanical Engineering, Georgia Institute of Technology, Atlanta, Georgia 30332, United States

[∇]School of Materials Science and Engineering, Georgia Institute of Technology, Atlanta, Georgia 30332, United States

[○]Department of Materials Science and Engineering, Clemson University, Clemson, South Carolina 29634, United States

S *Supporting Information*

ABSTRACT: High-performance lithium-ion batteries are commonly built with heterogeneous composite electrodes that combine multiple active components for serving various electrochemical and structural functions. Engineering these heterogeneous composite electrodes toward drastically improved battery performance is hinged on a fundamental understanding of the mechanisms of multiple active components and their synergy or trade-off effects. Herein, we report a rational design, fabrication, and understanding of yolk@shell Bi$_2$S$_3$@N-doped mesoporous carbon (C) composite anode, consisting of a Bi$_2$S$_3$ nanowire (NW) core within a hollow space surrounded by a thin shell of N-doped mesoporous C. This composite anode exhibits desirable rate performance and long cycle stability (700 cycles, 501 mAhg^{-1} at 1.0 Ag^{-1}, 85% capacity retention). By *in situ* transmission electron microscopy (TEM), X-ray diffraction, and NMR experiments and computational modeling, we elucidate the dominant mechanisms of the phase transformation, structural evolution, and lithiation kinetics of the Bi$_2$S$_3$ NWs anode. Our combined *in situ* TEM experiments and finite element simulations reveal that the hollow space between the Bi$_2$S$_3$ NWs core and carbon shell can effectively accommodate the lithiation-induced expansion of Bi$_2$S$_3$ NWs without cracking C shells. This work demonstrates an effective strategy of engineering the yolk@shell-architectured anodes and also sheds light onto harnessing the complex multistep reactions in metal sulfides to enable high-performance lithium-ion batteries.

KEYWORDS: lithium-ion battery, lithiation mechanism, yolk@shell composite anode, in situ experiments, multiple computational modeling
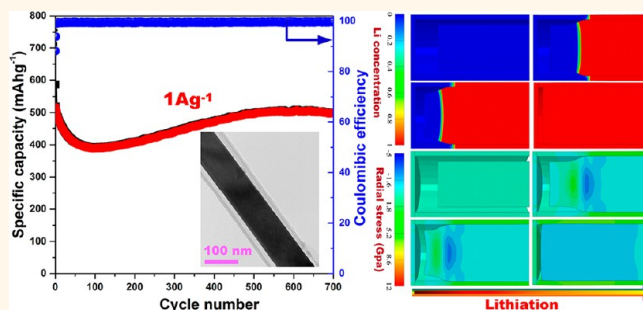
The fast-growing markets for portable electronic devices and hybrid electric vehicles have led to a strong demand of high-performance lithium-ion batteries (LIBs) with high energy density, fast charge/discharge rates, and long cycling life.[1−6] The electrochemical properties of LIBs depend critically on the performance of electrode materials.[7,8] Bismuth sulfide (Bi$_2$S$_3$) with a unique layer structure possesses the theoretical gravimetric capacity of 625 mAhg^{-1} (about 70% higher than that of graphite) and extremely high volumetric capacity of 4250 mAh cm^{-3}

(about four times that of graphite), respectively, and hence holds great potentiality as the alternative anode candidate for next-generation high-performance LIBs.[9−14] In particular, the space is usually limited for the power systems in compact electronic devices. Given its competitive volumetric capacity, Bi_2S_3 is a favored candidate anode material when high volumetric energy densities are desired for LIBs.[15] However, the dramatic volume changes of Bi_2S_3 during lithiation and delithiation can cause serious issues including cracking and pulverization of the Bi_2S_3 anode, loss of electrical contact with the current collector, and destruction and regeneration of the solid electrolyte interphases (SEIs) on the fractured surfaces of active Bi_2S_3. These issues inevitably lead to rapid capacity fading and hamper the widespread use of the Bi_2S_3 anode.[10,16]

Tremendous efforts have been devoted to resolving the aforementioned issues for better capacity retention and rate performance. Typical strategies include structural engineering of Bi_2S_3 into the nanoscale dimension (such as nanoparticles,[17] chrysanthemum-like nanostructures,[18] flower-like nanostructures,[19] etc.), fabrication of nanostructured Bi_2S_3-containing composites,[9,20,21] and engineering the hollow space.[16] Among these strategies, the surface coating has been proven effective for improving the electrochemical performance of electrode materials by changing their chemical and mechanical behaviors.[22,23] The coating can be used as a chemical barrier to separate the active materials from liquid electrolytes and to suppress the undesired side reactions between them, thereby stabilizing SEIs. It can also be used as a mechanically confining layer to restrain the volume changes during electrochemical cycling, thus mitigating the pulverization of active materials.[22−24] For example, carbon (C) coatings have been reported to enhance the cycling and rate performance of the electrode materials due to their high electrical and ionic conductivities and high mechanical strength as well as easy processing.[22] However, large volume changes from the combined conversion and alloying reactions of Bi_2S_3 upon lithiation can only be accommodated to a limited extent by C coating. Hence, only a modest improvement of cycling stability has been achieved by C coating so far.[25] Moreover, it is still a challenge to prevent capacity fading during prolonged cycling, since cracking and pulverization of the C coating may still occur upon repeated large volume expansions.[24] To overcome this challenge, fabrication of a yolk@C shell architecture would be helpful to enhance the cycling stability and rate performance. This is because the hollow space between the yolk and shell can accommodate the large volume expansion of the active yolk during lithiation without cracking the C shell. Meanwhile, the C shell can enhance the electrical and ionic transport and byproduct S after cycling could be overcome by its trapping effect.[24,26−28] However, the yolk@shell Bi_2S_3@C NW has not been reported yet. The effects of C coating and hollow space on the electrochemically induced mechanical performance remain unclear. Further, it is also unclear regarding the critical factors that control the capacity and cyclability of the yolk@shell anode. Hence, a fundamental study of lithiation mechanisms of the yolk@shell Bi_2S_3@C NW anode is necessary to clarify the above issues.

Here we report the rational design, fabrication, and fundamental understanding of Bi_2S_3@N-doped C yolk@shell NW anodes consisting of an active Bi_2S_3 NW core, an outer N-doped mesoporous C shell, and a hollow space in between the core and shell. By using in situ TEM, in situ selected area electron diffraction (SAED), in situ XRD, in situ NMR, and

computational model, we study the lithiation mechanisms, phase transformation, mechanical behaviors for the bare Bi_2S_3, core@shell Bi_2S_3@C NW, and yolk@shell Bi_2S_3@C NW electrodes. The as-prepared yolk@shell Bi_2S_3@C NW electrode integrates several favorable design attributes for high performance. (1) The hollow space can accommodate the large expansion of the active core without breaking the outer protective C shell,[24] which is confirmed by our in situ TEM measurement. (2) The outer permeable thin C shell offers effective electron conduction pathways for the Bi_2S_3 NW core. The C shell also reduces the polarization and electrochemical sintering of Bi_2S_3 NWs, rendering the uniform lithiation/delithiation of the NW ensemble.[23] An additional benefit is to prevent loss of electrical contact of the pulverized active materials by locking them inside the closed structure, thus maintaining the structural integrity,[24,26] as shown by our in situ TEM measurement and finite element analysis. In addition, the open mesoporous C shells with accessible channels ensure the complete immersion of active cores into the surrounding electrolyte, thus contributing to excellent rate capability.[24] Furthermore, N doping is utilized to modify the C shell, since this kind of doping has been shown to effectively improve the electrical conductivity, increase reactive sites, and favor electrode−electrolyte interactions.[29−31] Thanks to the above favorable attributes of the yolk@shell Bi_2S_3@C NW architecture, this composite electrode (Figure 1c) exhibits excellent performance and long cycling stability, such that it markedly outperforms both the bare Bi_2S_3 NW electrode
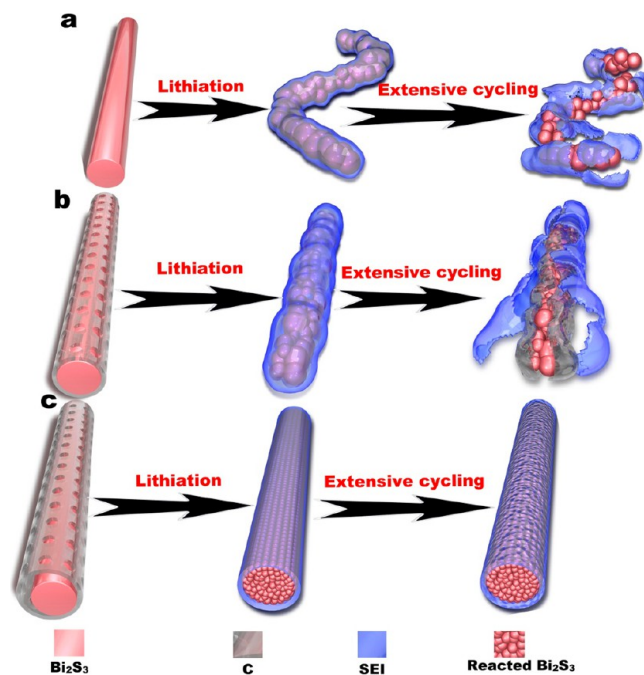
Figure 1. Schematic illustration of the lithiation process and repeated cycles of various Bi_2S_3-based anodes consisting of (a) bare Bi_2S_3 NW, (b) core@shell Bi_2S_3@C NW, and (c) yolk@shell Bi_2S_3@ C NW. The favorable design features of an outer N-doped mesoporous C shell, and a hollow space in between the Bi_2S_3 core and shell in yolk@shell Bi_2S_3@ C NW electrode can collectively contribute to mitigating the electrochemically induced mechanical degradation, thus enabling its long-cycle stability, while the bare Bi_2S_3 NW electrode and core@shell Bi_2S_3@C NW electrode are prone to mechanical degradation in both active components and SEIs during cycling.
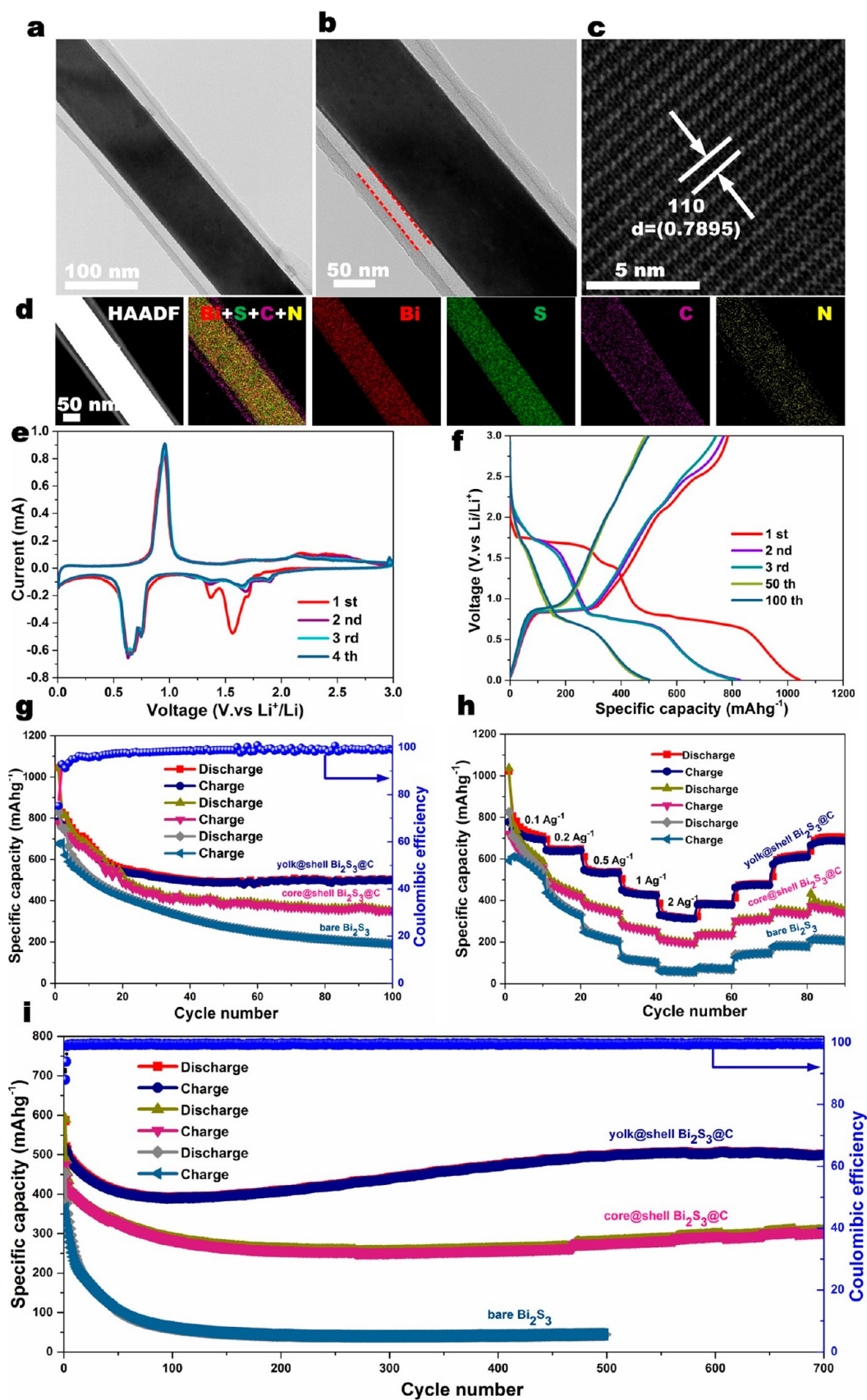
Figure 2. (a, b) TEM images of a single yolk@shell Bi_2S_3@C NW. (c) HRTEM image of Bi_2S_3 NW core. (d) STEM image and corresponding Bi, S, C, and N X-ray maps. (e) CV at a scan rate of 0.1 mV s^{-1} for yolk@shell Bi_2S_3@C NW electrode during the first four discharge/charge cycles. (f) Corresponding galvanostatic charge−discharge profiles at different cycles at a current density of 0.1 Ag^{-1}. (g) Cycling performance for yolk@shell Bi_2S_3@C, core@shell Bi_2S_3@C and bare Bi_2S_3 NW electrodes at 0.1 Ag^{-1}. (h) Rate performance of yolk@shell

C

Figure 2. continued

Bi$_2$S$_3$@C, core@shell Bi$_2$S$_3$@C and bare Bi$_2$S$_3$ NW electrodes at various current densities. (i) Long-cycle performance for yolk@shell Bi$_2$S$_3$@C, core@shell Bi$_2$S$_3$@C and bare Bi$_2$S$_3$ NW electrodes at 1 Ag^{-1}. all the electrodes are first tested at 0.1 Ag^{-1} for 5 cycles and then subjected to long-term cycling.

(Figure 1a) and the core@shell Bi$_2$S$_3$@C NW electrode (Figure 1b). Our findings shed light on the lithiation mechanisms and mechanical behaviors of heterogeneous composite electrodes that govern their electrochemical performance and offer crucial insights into the rational design of efficient and durable electrodes for high-performance LIBs.

RESULTS AND DISCUSSION

The processing route of void-containing mesoporous N-doped C, as used for encapsulating Bi$_2$S$_3$ NWs in the yolk@shell structures, is shown in Supplementary Figure S1. The Bi$_2$S$_3$ NWs are fabricated by hydrothermal treatment. The obtained single-crystal Bi$_2$S$_3$ NW with the smooth surface has a diameter about 120 nm (Supplementary Figure S2). Subsequently, a thin SiO$_2$ (Supplementary Figure S3) and C precursor layer are coated onto the Bi$_2$S$_3$ NWs by a two-step sol−gel coating method (Supplementary Figure S4). Finally, annealing under N$_2$ atmosphere together with subsequent etching results in the formation of yolk@shell Bi$_2$S$_3$@N-doped mesoporous C NWs (Figure 2a). It can be clearly observed that all the diffraction peaks in XRD patterns of bare Bi$_2$S$_3$ and yolk@shell Bi$_2$S$_3$@C NW samples are indexed as orthorhombic phase Bi$_2$S$_3$, which is accorded well with the standard card (JCPDS card no. 17-0320), indicating the high purity of the as-prepared Bi$_2$S$_3$ (Supplementary Figure S5). The TEM images in Figure 2a,b show that the Bi$_2$S$_3$ NW core is around 117 nm in diameter and entirely wrapped by the homogeneous C shells with an average thickness of ∼13 nm and a hollow space of ∼15 nm wide in between. Thermogravimetric analysis (TG) shows that the C content in yolk@shell Bi$_2$S$_3$@N-doped mesoporous C NWs is about 12 wt % (Supplementary Figure S6). The high-resolution TEM (HRTEM) image of the Bi$_2$S$_3$ NW core (Figure 2c) shows the clear and continuous lattice fringe with the neighboring fringe distance of 0.79 nm, which corresponds to the (110) interplane spacing of Bi$_2$S$_3$.[19] Figure 2d shows the TEM elemental mapping of yolk@shell Bi$_2$S$_3$@C NW. It is seen that Bi, S, C, and N elements are uniformly distributed in the composite matrix, confirming the conformal C coating on the Bi$_2$S$_3$ NW core.

To demonstrate the structural advantages of yolk@shell Bi$_2$S$_3$@N-doped mesoporous carbon NWs, cyclic voltammetric (CV) and galvanostatic charge−discharge (GCD) measurements are carried out to evaluate their Li storage performance with a coin cell configuration. The CV curves measured at a scan rate of 0.1 mVs^{-1} over the potential window of 0.01−3 V versus Li/Li$^+$ are shown in Figure 2e. During the first discharge, the peak at 1.57 V corresponds to the conversion of Bi$_2$S$_3$ to Li$_2$S and metallic Bi, and the subsequent two peaks at 0.76 and 0.64 V arise from the formation of LiBi and Li$_3$Bi alloys.[9] The peak at 1.37 V in the first discharge process, whereas disappearing during subsequent cycles, corresponds to the formation of SEIs. During the first charge, a sharp anodic peak at 0.96 V corresponds to the dealloying of Li$_3$Bi to metallic Bi, while the recovery of Bi$_2$S$_3$ is reflected by peaks at 2.18 and 2.40 V.[9] From the second cycle onward, all peaks are stable and reproducible, indicating the high reversibility of Li storage. Figure 2f and Supplementary Figure S7 show the typical GCD

profiles of the yolk@shell Bi$_2$S$_3$@C, bare Bi$_2$S$_3$, and core@shell Bi$_2$S$_3$@C NW electrodes tested at 0.1 Ag^{-1} between 3.0 and 0.01 V. The observed plateau in the first discharge curve represents the conversion and alloying reactions of Bi$_2$S$_3$ with Li, which is in accordance with CV results. The yolk@shell Bi$_2$S$_3$@C NW electrode delivers an initial discharge and charge capacity of 1044 mAhg^{-1} and 786 mAhg^{-1}, respectively, giving the first-cycle Coulombic efficiency of 75% (Figure 2f,g). The large capacity loss during the first cycle is likely caused by electrolyte decomposition and SEI film formation, but can be compensated by prelithiation through either chemical or electrochemical methods or by using stabilized Li metal powder.[16,32] It is worth noting that the specific capacity of the first discharge is higher than the theoretical capacity of bulk Bi$_2$S$_3$ (625 mAhg^{-1}). This phenomenon has been commonly observed in other metal sulfides anodes[33−35] and can be ascribed to the surface/interfacial Li storage,[36] SEI formation,[17] and the capacity contribution from amorphous C. A capacity of 504 mAhg^{-1} is achieved for the yolk@shell Bi$_2$S$_3$@C NW electrode after 100 cycles, which is higher than that of the core@shell Bi$_2$S$_3$@C NW electrode (352 mAhg^{-1} after 100 cycles) and the bare Bi$_2$S$_3$ NW electrode (192 mAhg^{-1} after 100 cycles) (Figure 2g). Strikingly, as shown in Figure 2h, the yolk@shell Bi$_2$S$_3$@C NW electrode exhibits significant enhancement on the rate performance as compared to that of the core@shell Bi$_2$S$_3$@C NW and bare Bi$_2$S$_3$ NW electrodes. The yolk@shell Bi$_2$S$_3$@C NW electrode delivers a high charge capacity up to 326 mAhg^{-1} at a high current density of 2 Ag^{-1} after 10 cycles, almost 1.6 times higher than that of the core@shell Bi$_2$S$_3$@C (209 mAhg^{-1} at 1 Ag^{-1}) electrode and 5.5 times higher than that of the bare Bi$_2$S$_3$ NW electrode (59 mAhg^{-1} at 1 Ag^{-1}). Interestingly, more than 90% specific capacity of the yolk@shell Bi$_2$S$_3$@C NW electrode can be readily restored when the current density is reduced to 0.1 Ag^{-1}, while only 46% and 29% specific capacity of the core@shell Bi$_2$S$_3$@C and bare Bi$_2$S$_3$ NW electrodes can be recovered, respectively (Figure 2h). To obtain the long-cycling results within a reasonable testing time, fast charge and discharge tests are carried out as shown in Figure 2i. It is observed that the yolk@shell Bi$_2$S$_3$@C NW electrode exhibits the best long-term cycling performance among all the electrodes. A specific capacity of 501 mAhg^{-1} with about 85% capacity retention of the yolk@shell Bi$_2$S$_3$@C NW electrode even after 700 cycles at a high current density of 1 Ag^{-1} can be achieved, which outperforms many reported results of Bi$_2$S$_3$-based anodes as shown in Supplementary Table S1. Under the same conditions, the core@shell Bi$_2$S$_3$@C NW electrode exhibits a significant decay of capacity, from 590 mAhg^{-1} during initial cycles to 287 mAhg^{-1} after 100 cycles, reaching a capacity of 306 mAhg^{-1} after 700 cycles with 61% capacity retention. The bare Bi$_2$S$_3$ NW electrode decays even more quickly, from 451 mAhg^{-1} during initial cycles to 61 mAhg^{-1} after 100 cycles, retaining a capacity of 44 mAhg^{-1} after 500 cycles with only 10% capacity retention. The high performance of the yolk@shell Bi$_2$S$_3$@C NW electrode can be reasonably associated with the beneficial effect of hollow space between the Bi$_2$S$_3$ NW core and C shell as well as that of the C shell for enhancing the electrode
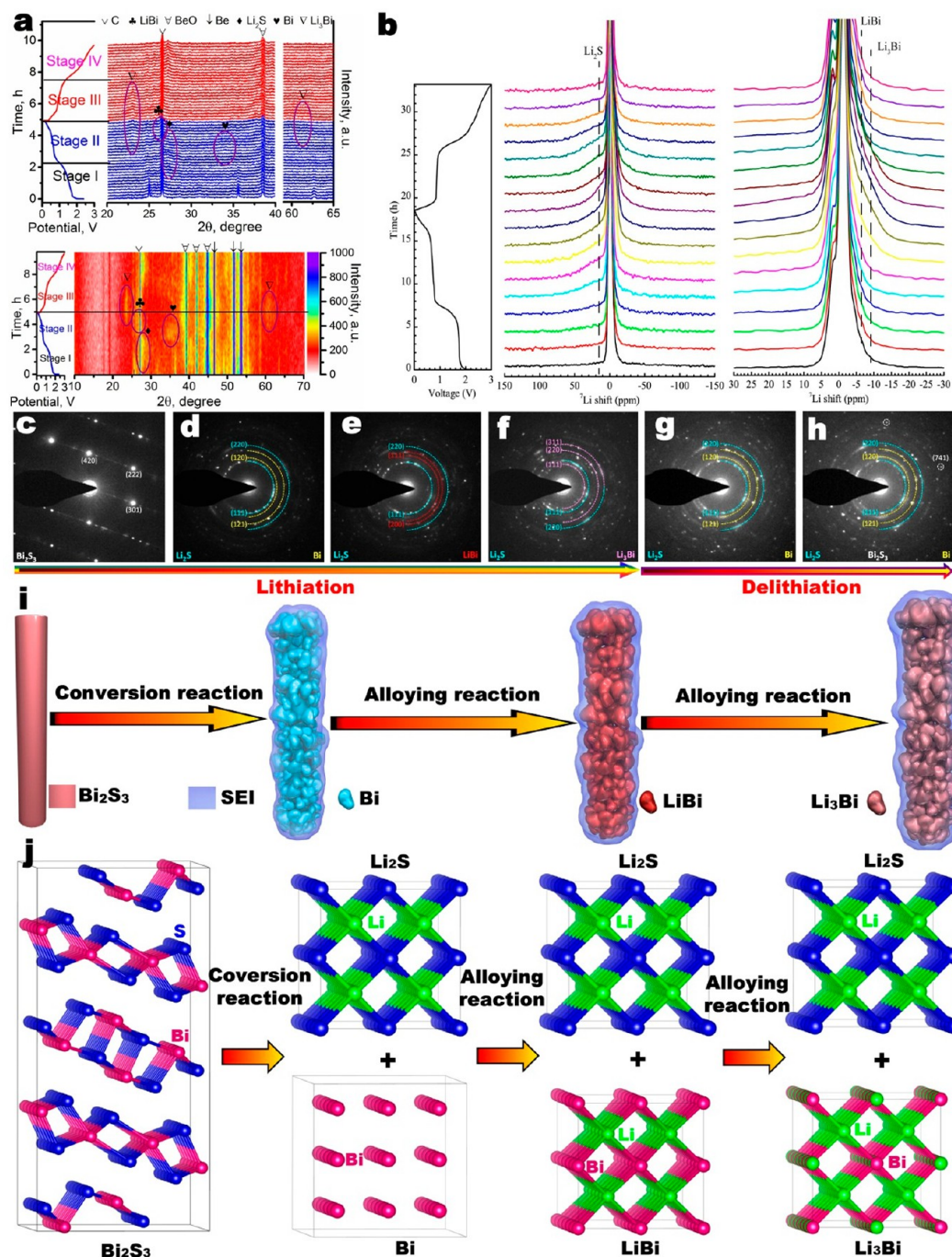
Figure 3. (a) Contour plot recorded at different lithiation/delithiation states against the electrochemical voltage during the initial cycle and XRD patterns within a selected 2 range during the first cycle against the voltage, electron diffraction intensity profile as a function of reaction time during lithiation and delithiation of bare Bi_2S_3 NW electrodes. (b) The real-time ^7Li NMR spectra in the first cycle between 0.01 and 3.0 V of bare Bi_2S_3 NW electrodes. Diffraction patterns of Bi_2S_3 NW before lithiation (c), during lithiation (d, e), after lithiation (f), during delithiation (g), and after delithiation (h). (i) Schematic of microstructural evolution and (j) atomic model of phase change and of Bi_2S_3 NW during lithiation.

stability and rate capability. In addition, the yolk@shell structure by itself is an advantageous geometry that can alleviate the expansion/contraction of Bi_2S_3 during discharge/charge.[24,26,37]

To gain insight into the Li storage mechanisms of Bi_2S_3 NW, *in situ* XRD and *in situ* NMR are performed upon lithiation/delithiation between 0.01 and 3.0 V. As shown in Figure 3a, Bi_2S_3 exhibits the characteristic peaks of (130), (221), (240), and (060) at 24.9°, 31.8°, 35.6°, and 48.2°, respectively.

Meanwhile, the peaks centered at 46.0°, 50.5°, and 52.5° are indexed as the Be window, and 26.5° is ascribed to the C paper in the *in situ* XRD cell.[38] When discharged from open circuit voltage (OCV) to 0.85 V, the standard peaks of Bi_2S_3 (PDF: 17−0320) are gradually weakened in intensity and finally disappear. Subsequently, two obvious peaks appearing around 27.0° and 33.4° are well indexed as Li_2S (PDF: 26-1188) and metallic Bi (0) (PDF: 26-0214), suggesting the conversion reaction of Bi_2S_3 with Li as well as the formation of Li_2S and Bi
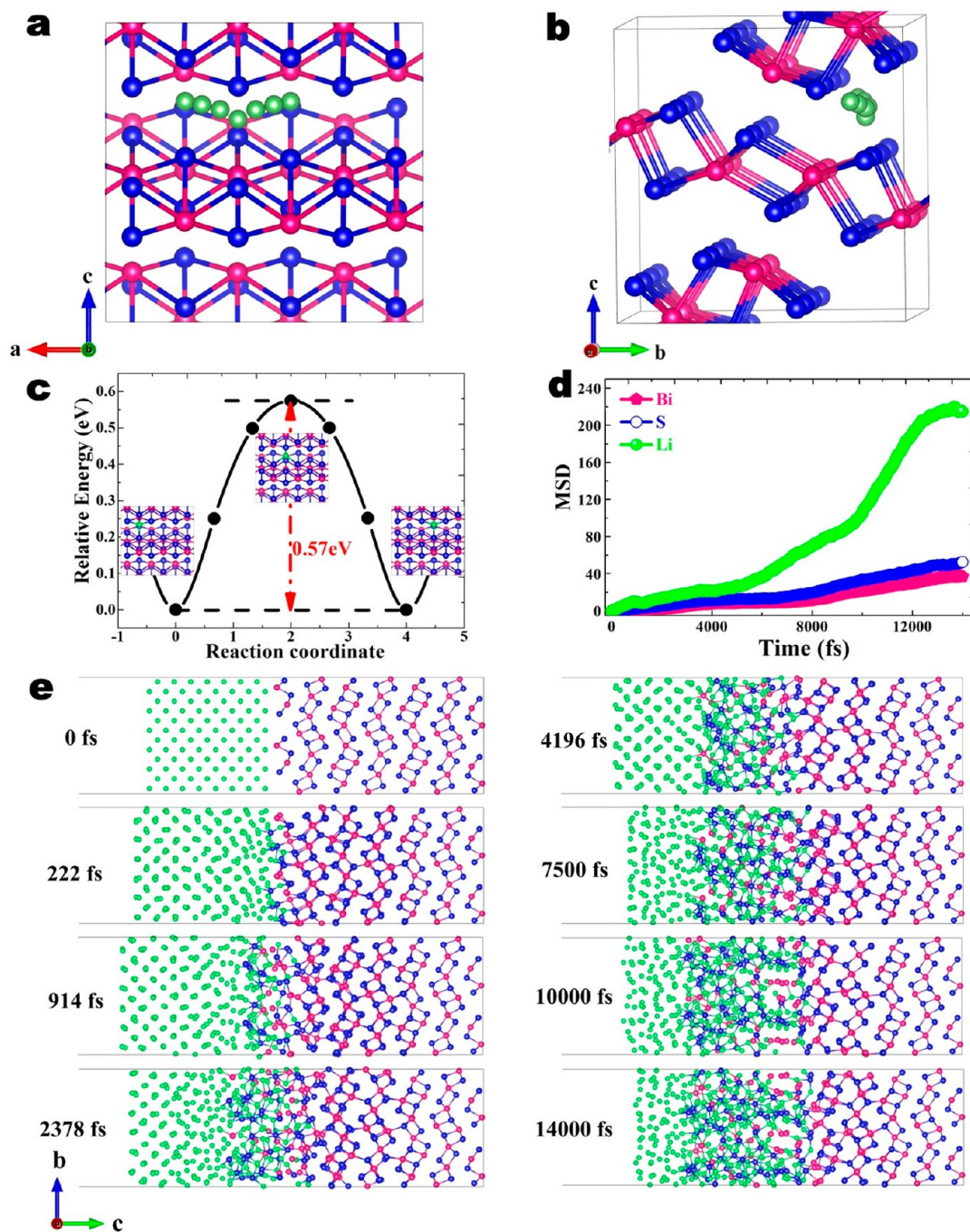
Figure 4. A Li diffusion path viewed from two different directions (a) and (b), where the seven cyan balls represent the optimized images for a single Li atom during the nudged elastic band calculation, and the corresponding minimum energy path of Li migration (c). (d) The MSD *versus* AIMD simulation time. (e) Snapshots of AIMD simulations. The red, blue, cyan balls represent Bi, S, and Li atoms, respectively.

(0); this phenomenon is similar to other chalcogenides.[39] Furthermore, when fully discharged to 0.01 V, the peaks of Li_2S and metallic Bi (0) gradually vanish along with an emerging new peak at 22.9° and about 26.5°, which is indexed to the formation of LiBi and Li_3Bi (PDF: 27-0427), confirming the Li insertion into metallic Bi (0) and the formation of the alloying product of LiBi and then Li_3Bi. During the corresponding charging cycle from 0.01 to 1.2 V, the peaks of Li_3Bi weaken and finally disappear, and the peaks of Li_2S are still observed, indicating the dealloying reaction of Li_3Bi to form Bi (0) metal. The low crystallinity phase of Bi_2S_3 restores after fully charged to 3.0 V, suggesting the partially reverse

conversion reaction between Li_2S and Bi (0) metal. Besides, the second cycle (Supplementary Figure S8a) shows similar structural evolution as the first cycle, confirming a completely reversible reaction process after the second cycle which is consistent with the results of GCD test and CV curves. The results indicate that the high capacity of Bi_2S_3 is related to the conversion reaction between Bi_2S_3 and Li as well as the alloying reaction between metallic Bi and Li. To confirm the structural evolution, a real-time ^{7}Li NMR spectrum in the first cycle between 0.01 and 3.0 V is conducted. As shown in Figure 3b, three new ^{7}Li NMR peaks around 6, −7, and −9 ppm are observed during cycling, and they correspond to the signal of

F

Li_2S, LiBi, and Li_3Bi, respectively. In the discharge process, the intensity of Li_2S increases until the discharge voltage approaches ~0.85 V. After that, the intensity of LiBi and Li_3Bi increases. The charge process exhibits a reverse process. To further shed light on the structural evolution of Bi_2S_3 NW during lithiation, *in situ* SAED measurement is performed (Figure 3c−h, captured from Supplementary Movies 1 and 2). When Li is inserted, the single-crystal SAED pattern of Bi_2S_3 (Figure 3c) transforms to the polycrystal SAED pattern (Figure 3d) with the emergence of diffraction rings from Li_2S and Bi, which is characteristic of the conversion reaction of Bi_2S_3 to Li_2S and Bi. Further lithiation brings about additional diffraction rings, whereas the rings of Li_2S still exist (Figure 3e,f). The additional ring can be attributed to the alloying reaction between Bi metal and Li and the formation of LiBi (Figure 3e) and then to Li_3Bi (Figure 3f). As the delithiation proceeded, the feature of Li_3Bi gradually disappeared, and the diffraction rings representing crystalline Bi increased and became clearer (Figure 3g), indicating the reversible dealloying reaction of Li_3Bi to Bi (0) metal, which is confirmed from the HRTEM image of bare Bi_2S_3 after delithiation (Supplementary Figure S9). Afterward, the diffraction rings/spots of Bi (0) metal decrease a bit, and a few diffuse rings representing Bi_2S_3 emerge (Figure 3h), while the rings of Li_2S are still present, in accordance with the *in situ* XRD results. This indicates that certain amounts of Li remains in the delithiated NW in the form of Li_2S due to the incomplete conversion of Bi to Bi_2S_3, resulting in an irreversible capacity loss during the first cycle as observed from the above CV and GCD results. The combined one-step conversion and two-step alloying reactions of Bi_2S_3 (Figure 3i) are in good accordance with the *in situ* XRD and NRM results obtained during lithiation. Based on our *in situ* XRD, *in situ* NMR, and *in situ* SAED results, we reveal that Bi_2S_3 may undergo one-step conversion reaction followed by two-step alloying reactions.[9] The first step represents the formation of metallic Bi and lithium sulfide by the following reaction:

$$Bi_2S_3 + 6Li \rightarrow 2Bi + 3Li_2S \qquad (1)$$

This reaction is irreversible. The subsequent two-step reactions are related to the reversible alloying reactions of metallic Bi with Li by the following reactions:

$$Li + Bi \rightarrow LiBi \qquad (2)$$

$$LiBi + 2Li \rightarrow Li_3Bi \qquad (3)$$

As expected, the phase transition recorded by *in situ* XRD, NMR, and SAED is related to the reactions discussed above. Therefore, the combined one-step conversion and two-step alloying reactions mechanism of the Bi_2S_3 electrode are confirmed by our *in situ* XRD, *in situ* NMR and *in situ* SAED experiments, which is in accordance well with the CV result. It should be noted that this reaction mechanism may not be observed in other metal sulfides with a layered structure such as MoS_2,[40] in which a reversible intercalation step occurring at the potential ranging from 3 to 1.1 V (*vs* Li/Li^+), forming crystalline Li_xMoS_2 followed by a conversion reaction of Li_xMoS_2 to Li_2S and Mo. The lithium−sulfur redox couple dominates the subsequent cycling process of MoS_2,[39] whereas the Bi−Li reaction prevails in the Bi_2S_3 electrode that governs the subsequent charging and discharging processes. These types of reaction mechanisms in metal sulfides indicate the importance of a clear understanding of the reaction process in individual electrode materials. In the second lithiation/delithiation process (Supplementary Figure S8b), a similar structural evolution occurs and is consistent with the *in situ* XRD result of the second cycles. The thermodynamics of Li intercalation is considered by constructing the equilibrium Li−S−Bi ternary phase diagram based on density functional theory (DFT) calculations. As shown in Supplementary Figure S10, the dashed line connecting Li and Bi_2S_3 indicates the conditions relevant to lithiation/delithiation of the Bi_2S_3 anode. The atomistic model and the schematic of microstructural evolution during the two-step reaction of Bi_2S_3 NWs are shown in Figure 3i,j, respectively.

DFT calculations are performed to understand the lithiation kinetics at the atomic level.[41] During the early stage of lithiation, Li enters the Bi_2S_3 lattice through diffusion. We investigate the Li diffusion capability by computing the Li migration barriers. Three Li diffusion paths are examined. The respective migration path in the lattice and the associated minimum energy path are shown in Figure 4a−c. The interstitial sites of Li in the initial and final states of a diffusion process are translationally invariant along the *b*-axis, while the interstitial Li site at the transition state is located in the middle of the diffusion path. Along the *b*-axis of the Bi_2S_3 lattice, large diffusion channels can be geometrically identified. This facilitates the finding of an easy Li diffusion path with a low-energy barrier. From DFT calculations, the lowest energy barrier from the initial to the final state is 0.57 eV, whereas the energy barriers for the other two paths are 1.22 eV (Supplementary Figure S17), indicating that Li mainly diffuses through the channels along the *b*-axis or the $(Bi_4S_6)_n$ moiety direction of the Bi_2S_3 crystal. The low-energy barrier of Li diffusion from DFT is comparable to the reported values for $LiMnPO_4$ (0.60 eV),[42] bulk Bi_2MoO_6 (~0.40 eV),[43] and $LiFePO_4$ (0.48 eV),[42] and it is also consistent with the fast rate of initial Li intercalation. The high diffusivity can be related to the weak van der Waals (vdW) interactions between $(Bi_4S_6)_n$ moieties in the Bi_2S_3 crystal. In other words, the weak vdW interactions facilitate the formation of fast channels of Li diffusion.

To further understand the lithiation reactions and confirm the lithiation mechanisms identified *via in situ* XRD, *in situ* NMR, and *in situ* SAED measurements, *ab initio* molecular dynamics (AIMD) simulations are performed to study the dynamic process of Li intercalation. To construct the atomic model, a DFT-optimized Bi_2S_3 slab structure is interfaced with a pure Li slab with an interslab distance of 2.1 Å (see Figure 4e). We calculate the respective mean squared displacement (MSD) of Li, Bi, and S atoms during AIMD simulations.[44,45] That is,

$$MSD = \langle (x - x_0)^2 \rangle = \frac{1}{N} \sum_{n=1}^{N} (x_n(t) - x_n(0))^2 \qquad (4)$$

where N is the number of atoms, $x_n(0)$ is the reference position of each atom, $x_n(t)$ is the position of each atom at time t. As shown in Figure 4d, the slope of the MSD curve for Li atoms is greater than that of S and Bi atoms, indicating that the Li diffuses much faster than S and Bi during lithiation. The time series of AIMD snapshots are shown in Figure 4e. Specifically, the initial configuration in the AIMD simulation is shown at 0 fs. At 222 fs, the Li enters the Bi_2S_3 crystal immediately after the start of the AIMD simulation, and then Li is bonded with S to form lithium sulfide, while Bi atoms
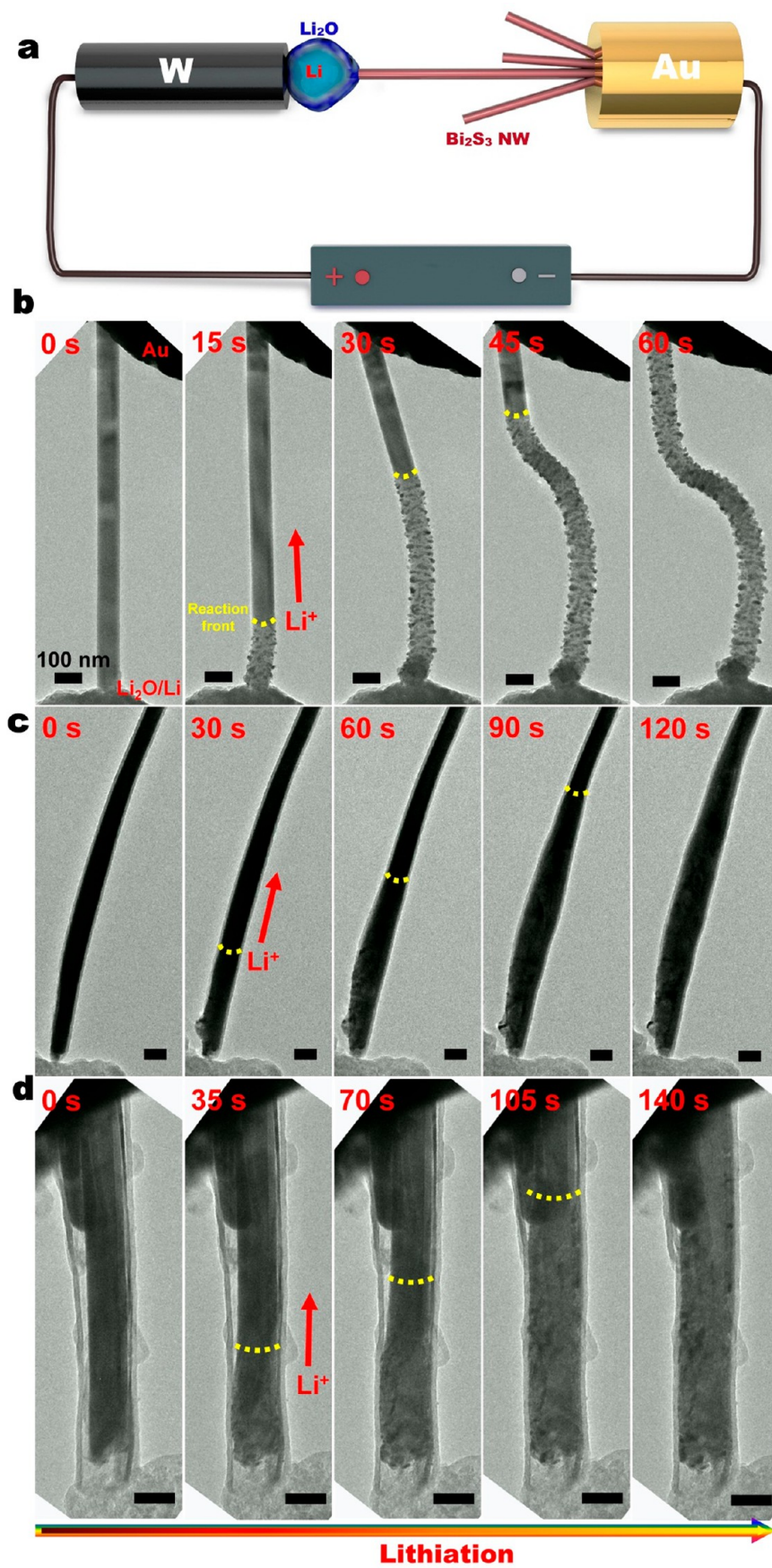
Figure 5. (a) Schematic illustration of the *in situ* nanobattery setup. Time-lapse TEM images for (b) bare Bi$_2$S$_3$ NW, (c) core@shell Bi$_2$S$_3$@C NW, and (d) yolk@shell Bi$_2$S$_3$@C NW during lithiation process.
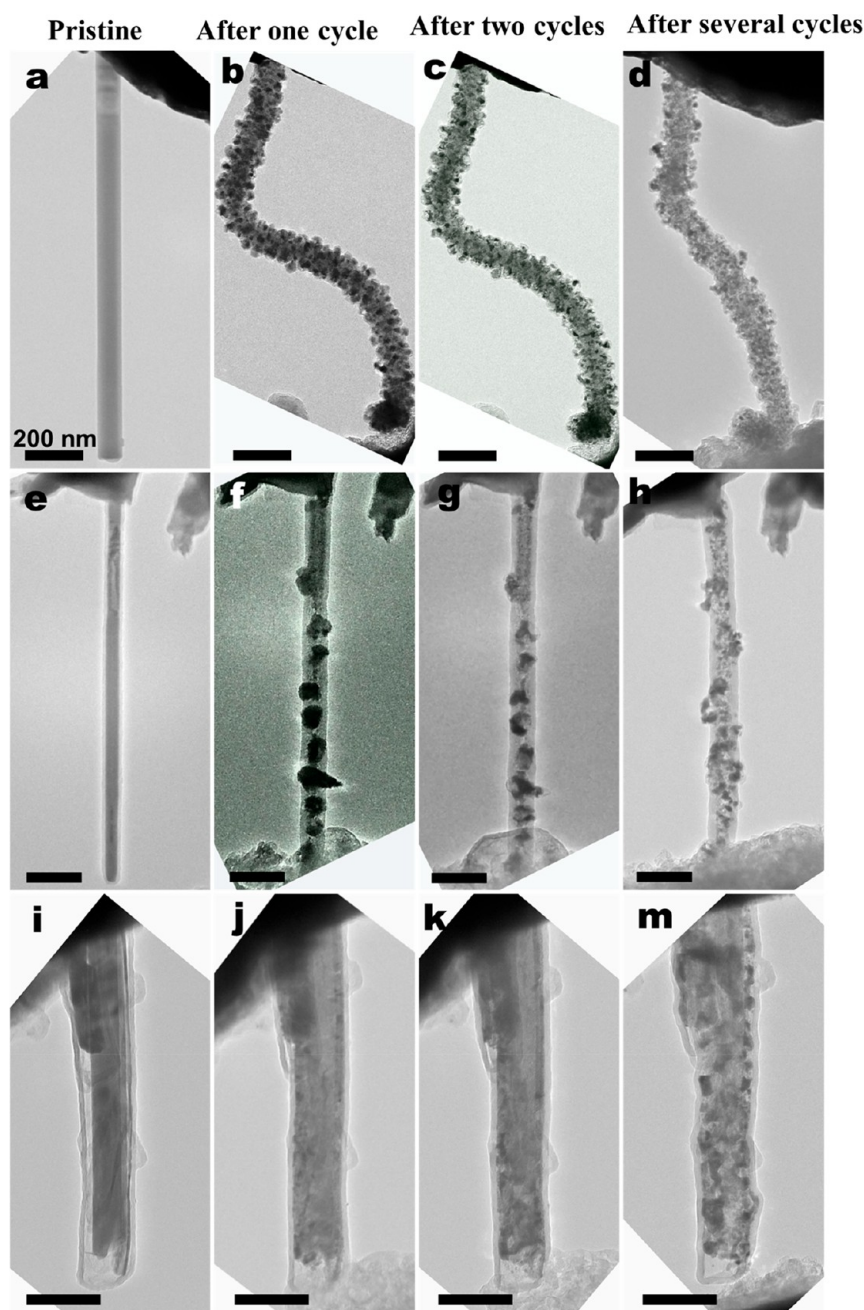
Figure 6. *In situ* TEM images of a single (a) pristine bare Bi_2S_3 NW (b) after one cycle (c) after two cycles and (d) after several cycles. (e) Pristine core@shell Bi_2S_3@C NW, (f) after one cycle (g) after two cycles and (i) after several cycles. (i) Pristine yolk@shell Bi_2S_3@C NW, (j) after one cycle, (k) after two cycles (m) after several cycles.

become isolated (nonbonded). As more Li diffuses into the crystal, large lattice distortion occurs, leading to the formation of amorphous Bi_2S_3. During this process, for example, at 2378 fs, Bi atoms in the intercalated regions start to bond with Li atoms to form lithium bismuth, coexisting with lithium sulfide. This behavior is consistent with the experimental observation shown in Figure 3. Interestingly, the volume of the simulation system expands from 0 to 914 fs due to the amorphization process of the interfacial atoms, and this is followed by the volume contraction with the further diffusion of Li into Bi_2S_3.

To gain a deep understanding on the electrochemical behavior of bare Bi_2S_3, core@shell B_2S_3@C and yolk@shell Bi_2S_3@C NW electrodes in LIBs, the lithiation process of the three types of NWs is investigated by *in situ* TEM through a

nanobattery configuration as schematically shown in Figure 5a.[46−48] Figure 5b shows the time-lapse TEM images of morphological evolution of a Bi_2S_3 NW without C coating during lithiation (captured from Supplementary Movie 3). The pristine Bi_2S_3 NW is initially straight and uniform along the radial direction (Figure 5b). When a potential of −3.0 V is applied to the Bi_2S_3 NW with respect to the counter electrode of Li metal, Li begins to diffuse into one end of the NW through the Li_2O layer formed on the surface of Li metal. The subsequent Li diffusion and lithiation process can be visualized by the propagation of the reaction front along the nanowire, as marked with the yellow dash line that indicates the boundary separating the lithiated (undergoing a large swelling) and unlithiated parts. There is no apparent dislocation cloud or

nanowire cracking found at the reaction front, which differs from the lithiation process of SnO_2,[49] ZnO,[50] and RuO_2 NWs.[51] The ripples ahead of the reaction front are likely due to the stress-induced contrast in the TEM images. As the reaction fronts propagate from the bottom to the top, the Bi_2S_3 NW becomes swelled and curved (Figure 5b), which are caused by the expansion in both radial and axial directions. Meanwhile, the microstructure of the Bi_2S_3 NW evolves from single crystal to polycrystal containing numerous Bi nanograins embedded in the Li_2S matrix, showing the characteristic of the conversion reaction from Bi_2S_3 to Bi and Li_2S. Further lithiation induces the expansion of Bi nanograins due to the alloying reaction between Bi and Li (Supplementary Figure S11). It is difficult to observe the dynamic Li−Bi alloying reaction since it happens too fast to be identified within each alloying nanograin. After lithiation, the reacted part expands in diameter by ∼23.6% and also elongates significantly causing the NW to curve. It is worth noting that the reaction front maintains a conical shape during the whole lithiation process, suggesting the concurrent lithiation along both the radial and axial directions.[52] Supplementary Figure S12a shows an HRTEM image of the lithiated Bi_2S_3 NW, which features many nanograins of ∼7 nm in size and a thin layer of ∼4 nm in thickness formed on the NW surface. In a few nanograins, the lattice spacing of 0.339 nm is found to match the (200) plane of the crystalline Li_3Bi alloy (PDF: 27-0427), while the fringe spacing of 0.330 nm can be indexed as the (111) planes of Li_2S (PDF: 26-1188).[53] The SAED pattern (Supplementary Figure S12b) of the lithiated Bi_2S_3 NW also demonstrates the formation of Li_2S involved in the lithiation reaction, which accompanies the alloying reaction of Bi and Li to form Li_xBi (Li_3Bi). The scanning TEM (STEM) image combined with energy dispersive X-ray (EDX) spectroscopy mapping analysis (Supplementary Figure S12c) confirms the formation of a composite framework that consists of crystalline Li_xBi nanograins dispersed in the Li_2S matrix after the first lithiation of the Bi_2S_3 NW.

Interestingly, the lithiation behavior of C-coated Bi_2S_3 NWs differs notably from that of the bare NWs. Figure 5c shows the time-lapse TEM images of the lithiation process of a C-coated Bi_2S_3 NW (captured from Supplementary Movie 4). There is no detectable axial expansion, but the NW can expand along the radial direction by ∼52.8% (at the most expanded section) eventually. This contrasts with the free lithiation process of the bare NW, in which both radial expansion and axial elongation occur. Furthermore, different from the bare Bi_2S_3 NW, no distinct contrast between the lithiated and unlithiated regions is observed around the reaction front (marked by the yellow dashed line, Figure 5c). The suppression of longitudinal expansion in the C-coated NW is likely caused by the mechanical confinement of the surface C layer.[23] Impressively, the yolk@shell structure does not exhibit significant expansion (with a minimal radial expansion of ∼6.2%, defined by the diameter of carbon shell) during lithiation (Figure 5d) (captured from Supplementary Movie 5). Similar to the lithiation of core@shell B_2S_3@C NW, we do not observe apparent axial elongation or distinct contrast at the reaction front of yolk@shell Bi_2S_3@C NW. Although the encapsulated Bi_2S_3 NW also experiences drastic volume changes during the progression of lithiation, the void space between the Bi_2S_3 NW and C shell can accommodate the full expansion of the Bi_2S_3 NW without cracking the C shell. Hence, the yolk@shell structure can effectively buffer the volume change of Bi_2S_3.

This is beneficial to the macroscopic electrochemical properties of yolk@shell Bi_2S_3@C NW electrode, as reported earlier in this paper.

To understand the lithiation/delithiation behavior of the three types of NWs upon repeated cycling, we record their morphological evolution in the first few cycles, and Figure 6 shows the results after the first, second, and several cycles, respectively. As shown in Figure 6a−c (captured from Supplementary Movie 6), fast lithiation/delithiation (by applying an −6/6 V bias) transforms the initially straight Bi_2S_3 NW into a curved and phase-segregated structure, decorated with particle-like products embedded in the Li_2S matrix. After several cycles, the bare Bi_2S_3 NW exhibits drastic structural changes and becomes highly fluffy morphology with many cracks on the surface. As for the core@shell B_2S_3@C NW, although it can maintain its straight shape upon fast lithiation, the rapid radial expansion of the Bi_2S_3 core leads to the carbon shell cracking due to the lack of void space inside the shell (Supplementary Figure S13 and Figure S14). The NW is not able to restore its original morphology by shrinking back of the lithiated Bi_2S_3 into the C shell after delithiation (Figure 6f), thus causing poor structural stability under high rates. During subsequent lithiation/delithiation cycling (Figure 6g,h, captured from Supplementary Movie 7), due to the lack of effective confinement from the C coating, these extruded products experience volume expansion and shrinkage and collapse into many small pieces with numerous surface cracks, leading to poor structural integrity after cycling.

Impressively, the C coating of the yolk@shell structure can (Figure 6i−m, captured from Supplementary Movie 8), to the maximum extent, preserve its structural integrity, except that the hollow cavity is fully filled with the lithiated Bi_2S_3 under fast lithiation/delithiation cycling. This observation indicates that the yolk@shell structure can effectively mitigate the lithiation-induced swelling of Bi_2S_3. Such lithiation/delithiation behavior of the yolk@shell Bi_2S_3@C NW can be repeated for several times without any unstable structural changes, such as cracking and fracture (Supplementary Figure S15). Interestingly, the particle-like products produced from the first lithiation/delithiation of Bi_2S_3 core exhibit reversible volume expansion and contraction inside the C shell (Supplementary Movie 8), suggesting that the yolk@shell Bi_2S_3@C NW electrode could be effectively used for high-cycle applications in LIBs. Although the Bi_2S_3 NW core also experiences large volume changes and structural fragmentation during lithiation/delithiation cycling, the active materials are retained in the C shell (Figure 6m). This suggests that the yolk@shell structure is also helpful to mitigate the pulverization of Bi_2S_3 NWs. In addition to the benefit from the hollow void, the C shell can enhance electronic/ionic transport and act as a protective layer to prevent the core material from losing electric contact with the yolk@shell Bi_2S_3@C NW electrode. The aforementioned factors can collectively contribute to mitigating the electrochemically induced mechanical degradation, thereby enhancing the long-cycle structural stability and rate capability as verified by the excellent macroscopic electrochemical performance of the yolk@shell Bi_2S_3@C electrode. To further confirm the *in situ* TEM results, we performed the ex-TEM observation (Supplementary Figure S16) of the structural change of these three electrodes at 0.1 Ag^{-1} for 100 cycles as discussed above. The whole NW structure of yolk@shell Bi_2S_3@C NW (Supplementary Figure S16e−l) electrode is well retained without drastic morphological changes, and the hollow space is
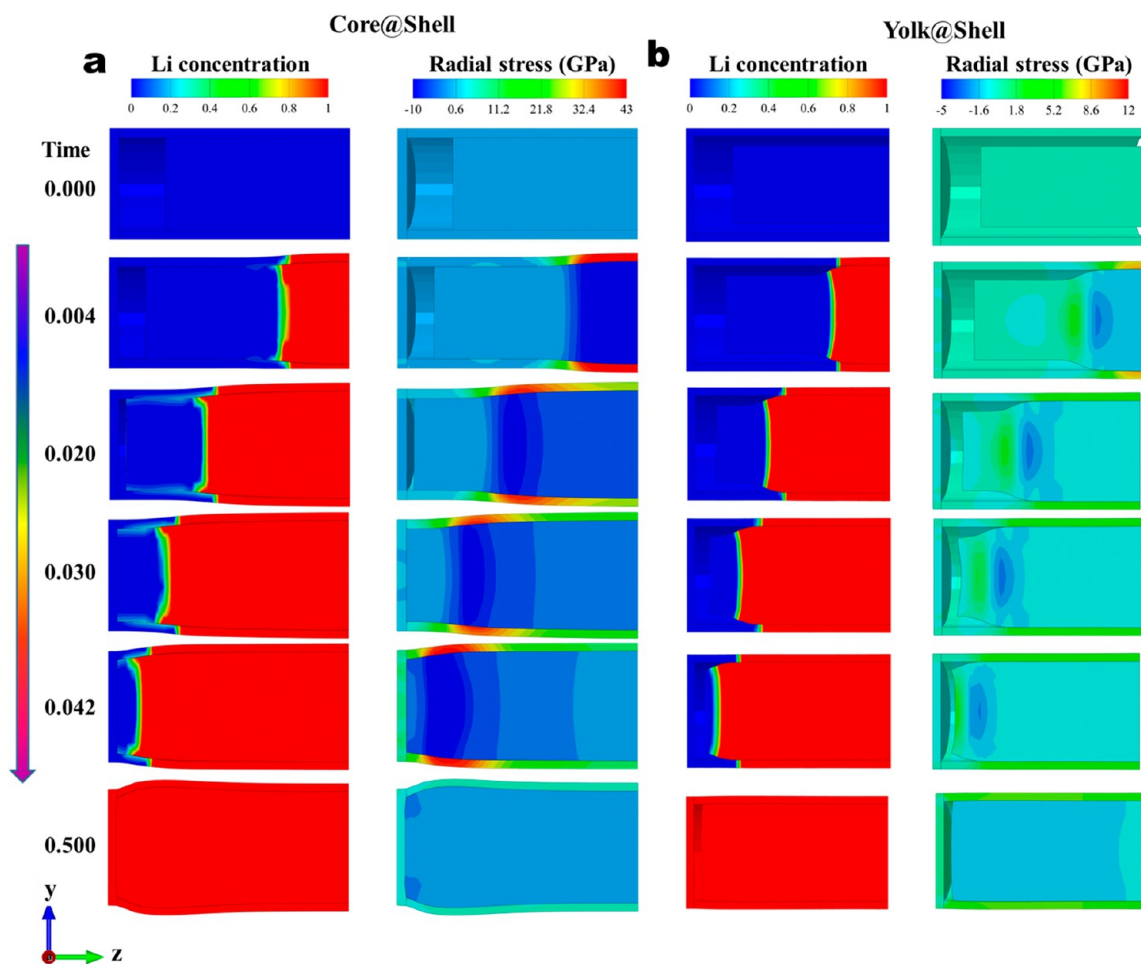
Figure 7. Finite element simulation results of Li diffusion and associated elastic-plastic deformation, showing the Li distribution and radial stress distribution in (a) a core@shell NW and (b) a yolk@shell NW.

filled with lithiated Bi_2S_3, demonstrating a good structural integrity after long-term cycling. In contrast, both the bare Bi_2S_3 NW (Supplementary Figure S16a,b) and core@shell Bi_2S_3@C NW (Supplementary Figure S16c,d) electrodes experience the marked structural changes such as cracking and fracture, indicating a poor structural integrity after long-term cycling. This result correlates well with the *in situ* TEM results.

To understand the *in situ* TEM results, we perform the continuum chemomechanical simulations using the yolk@shell and core@shell structure models. The simulations co-evolve the Li diffusion and elasto-plastic deformation using the finite element method.[23,54−59] The results provide insights into the mechanistic origin of the improved electrochemical cycle performance. Specifically, the lithiation-induced plastic deformation is assumed to obey the classic J_2 flow rule.[60] The normalized Li concentration, c_{Li}, is defined as the local Li concentration divided by the Li concentration of the fully lithiated state. The lithiation reaction front coincides with the interface between the pristine (blue) and lithiated (red) phases (see Figure 7). Figure 7a,b shows the simulated Li distribution and corresponding radial stress distribution in the core@shell NW and yolk@shell NW, respectively (Supplementary Movies 9 and 10). The configurations in Figure 7 at time $t = 0$ show the pristine core@shell and yolk@shell model, respectively. As the lithiation proceeds, the Li diffuses from the right to the left

end, and a sharp lithiation front (*i.e.*, phase boundary) is obtained in the simulation. This lithiation reaction front propagates along the axial direction. Due to the mechanical constraint of the C coating in the core@shell model (Figure 7a), radial expansion of the wire can be almost entirely suppressed. In this case, the radial tensile stress ahead of the reaction front is reduced to nearly zero in the shell, whereas a large radial compressive stress develops behind the reaction front. Such an abrupt change from the radial tensile stress in the shell and the radial compressive stress in the core causes a large stress concentration, which could lead to the decrease of long-cycle stability of the coated Bi_2S_3 NW electrode in experiments. To compare the radial stress more clearly, a smaller range of color map is used for the yolk@shell structure (Figure 7b) than that for the core@shell structure (Figure 7a). In contrast to the core@shell model in Figure 7a, Figure 7b shows the simulated Li distributions and associated radial stress distributions (Supplementary Movies 11 and 12). The maximum radial stress of 43 GPa of the core@shell model is almost 5 times that of the yolk@shell model (8.6 GPa), which could cause severe stress concentrations and thus pulverization of the C shell. These results agree well with the experimental observation shown in Figure 6. They also suggest possible means to improve the long-cycle stability. First, the tensile stress in the shell of the core@shell model can be greatly relieved in the yolk@shell model. This drastic change is

attributed to the hollow space of the yolk@shell model, which provides free space to accommodate the lithiation-induced expansion of the core. Second, since there is a C shell outside the Bi_2S_3 NW, the Bi_2S_3 core cannot expand freely. This could alleviate the fragmentation and loss of electrical contact. Overall, compared to the core@shell structure, the yolk@shell structure can not only suppress the radial expansion in the lithiated Bi_2S_3 NW but also retain its structural integrity.

CONCLUSIONS

We have systematically studied the effects of the bare (*i.e.*, without coating), core@shell, and yolk@shell structures on the lithiation behavior of Bi_2S_3 NWs. The electrochemical and mechanical behaviors of these structures are characterized in real time by a suite of experimental techniques. The *in situ* XRD, *in situ* NMR, and *in situ* SAED measurements reveal that Li storage in Bi_2S_3 involves the conversion and alloying reactions. The *in situ* TEM observations indicate that the hollow space in between the C shell and the Bi_2S_3 NW core not only provides adequate room to accommodate the radial expansion of Bi_2S_3 during lithiation without cracking the C shell but also maintains the yolk@shell structural integrity by alleviating the degradation of SEIs on the outer surface of the C shell. The DFT calculations show the low Li diffusion barrier of 0.57 eV in the Bi_2S_3 lattice, and the AIMD simulations shed light onto the atomistic dynamic lithiation processes near the reaction front. The finite element simulations of the lithiation process and associated elastic-plastic deformation reveal the lithiation-induced stress concentration near the reaction front. These simulations also indicate that the yolk@shell structure can effectively alleviate stress concentrations and suppress radial expansions during lithiation. Owing to these unique structural characteristics and benefits, the yolk@shell Bi_2S_3@C NW electrodes exhibit the high rate capability and long cycle stability. Our findings provide mechanistic insights into the rational design and fabrication of high-performance and durable anodes for advanced LIBs.

METHODS

Synthesis of Bi_2S_3 NWs. The synthesis of the Bi_2S_3 NW involves the following steps: 3 g $LiNO_3$ and 6 g KNO_3 are placed in a 30 mL Teflon vessel as the solvent, and then 1 mmol $Bi(NO_3)_3 \cdot 5H_2O$ and 4 mmol $Na_2S \cdot 9H_2O$ are also put into the Teflon vessel. The vessel is shaken to ensure the full mixing of reactants, and 5 mL ultrapure water is added into the vessel to adjust the viscosity of the melts. Then the Teflon vessel is sealed in a stainless autoclave and heated at 200 °C for 72 h. After reactions, the vessel is taken out and allowed to cool down to room temperature naturally. The product is washed with deionized water and ethanol and finally collected after drying at 60 °C for 6 h.

Synthesis of Bi_2S_3@SiO_2 Core@Shell NWs. In a typical synthesis, 0.5 g as-obtained Bi_2S_3 NWs are well dispersed in 194 mL isopropyl alcohol after 30 min ultrasonication and 10 min stirring, followed by adding 18 mL H_2O, 10 mL NH_4OH, and 0.2 mL tetraethyl orthosilicate (TEOS) to the beaker. The dispersion is further stirred for 2 h at 40 °C. Hereafter, the core@shell Bi_2S_3@SiO_2 core@shell NWs are fabricated after centrifugation and washing with ethanol several times.

Synthesis of Yolk@Shell Bi_2S_3@N-Doped C NWs. Bi_2S_3@SiO_2 core@shell nanowires (1 g) are dispersed in a mixture of ethanol (60 mL) and H_2O (140 mL). After the addition of resorcinol, formaldehyde, ethylenediamine (EDA), and TEOS in sequence, the mixed solution is stirred at 30 °C for 24 h. Here, EDA can be used as the N-doped agent, while TEOS derived SiO_2 can be regarded as a convenient pore-forming agent.[61] The obtained intermediates Bi_2S_3@

SiO_2@polybenzoxazine(PB)/SiO_2 are collected by centrifugation. These intermediates are further dried and then carbonized under an N_2 atmosphere at 400 °C for 4 h. Finally, yolk@shell Bi_2S_3@C NW is prepared after the removal of silica using 1.0 M NaOH aqueous solution. The dosages of Bi_2S_3@SiO_2/resorcinol/formaldehyde/EDA/TEOS used in the synthesis are 1 g/0.64 g/0.96 mL/0.64 mL/0.3 mL, respectively.

Material Characterization. The morphology and microstructure of the as-prepared samples are studied by field-emission scanning electron microscope (FE-SEM, Hitachi SU-70, Tokyo, Japan) and high-resolution transmission electron microscopy (HRTEM, FEI, Talos 200s) operating at 200 kV. The crystalline structure is indexed by X-ray diffraction on a Bruker D8 Advanced X-ray diffractometer (Cu−Kα, λ = 1.5418 Å).

In Situ XRD Measurement. The *in situ* XRD investigation is performed on a live lithiation/delithiation process (at a current density of 0.15Ag^{-1}) in a homemade cell. The XRD chamber is sealed by a Be foil to allow X-ray transition and equipped with carbon paper as a current collector. During the electrochemical measurement, each scan of the XRD pattern is collected in the 2θ range of 20−70° with a 0.02° step increment at a scanning rate of 0.08° s^{-1}.

In Situ TEM Observation. The lithiation/delithiation processes are observed by *in situ* TEM using the Nanofactory TEM holder operated at 200 kV. Yolk@shell Bi_2S_3@C NWs are loaded on an Au tip and then connected to Li/Li_2O on a W tip. The native Li_2O on the Li surface serves as a solid electrolyte. Lithiation of an individual NW initiates once a negative voltage is applied to the W end, whereas delithiation starts off upon reversing the signal of the voltage bias.

In Situ NMR Characterization. The *in situ* ^{7}Li NMR experiments are performed with a Bruker Avance III 600 MHz spectrometer, operating at ^{7}Li resonance frequency of 233.3 MHz. The *in situ* cell is assembled in an argon-filled glovebox and cycled at a current of 40 mA g^{-1} during the *in situ* NMR test. The *in situ* ^{7}Li NMR spectra are acquired using a single pulse method with a pulse length of 3 μs and a recycle delay of 2 s, referencing to 1 M LiCl aqueous solution (0 ppm). The *in situ* NMR spectra are recorded per hour.

Electrochemical Measurement. The electrochemical properties of the as-prepared anodes are measured by using the CR2025 coin-type cell. The working electrode is mixed by yolk@shell Bi_2S_3@C NWs (80 wt %) with conductive carbon black (10 wt %) and binder polyvinylidene fluoride (10 wt %) in an *N*-methyl pyrrolidone (NMP) solvent. The diameter of the electrode is cast into 14 mm tablet, while the typical mass loading of the working electrode is 1.0−1.5 mg cm^{-2}. A metallic Li metal foil (15 mm in diameter) and 1 M $LiPF_6$ (EC:DMC:EMC = 1:1:1, in volume with 5% FEC) are used as the counter electrode and the electrolyte, respectively. The galvanostatic discharge/charge tests are performed on Land CT2001A system (Wuhan, China) at room temperature, while the mass-specific capacity is calculated according to the mass of active material. The cyclic voltammetry (CV) is performed on a four-channel multifunctional electrochemical workstation (VersaSTAT MC, America), and scanning is conducted from 3 to 0.01 V *versus* Li/Li$^+$ at a rate of 0.1 mV s^{-1}.

DFT and AIMD Modeling. DFT calculations are performed with the generalized gradient approximation (GGA) in the form of the Perdew−Burke−Ernzerhof (PBE) functional as implemented in the Vienna *ab Initio* Simulation package (VASP) 5.4.[62] The kinetic cutoff for plane-waves is set at 520 eV. The reciprocal space is sampled on the γ centered meshes with a density larger than 10/Å. The convergence criterion for electronic self-consistent calculations is 10^{-5} eV. Both the atomic positions and the lattice parameters are allowed to change during structural relaxation until the Hellmann−Feynman forces on each atom are lower than 10^{-2} eV Å^{-1}. For AIMD simulations, we use the hybrid Gaussian and plane waves method as implemented in the Quickstep module of the CP2K package[63] to improve the computational efficiency. The PBE functional with the Grimme correction scheme is employed for calculating the electronic structure properties.[64] The DZVP-MOLOPT-SR-GTH basis set in combination with GTH pseudopotentials is utilized for all atoms.[65] The time step is set as 2 fs, and the simulation is carried out using the

canonical ensemble (NVT) with an optimized initial structure. The temperature of the simulation system is controlled at 700 K. The diffusion barriers of Li in different crystalline phases are calculated using the climbing image nudged elastic band method in the VASP package.[64] The Bader charge analysis for the single Li atom shown in Figure 4a system suggests that Li losses ~0.83 e charge. The phase diagram is generated using the Python Materials Genomics (Pymatgen) based on the *ab initio* data bank "materials project".[65,66]

Finite Element Modeling. To understand the coupling of lithiation and stress generation, the time-dependent two-phase lithiation process is simulated by combining a nonlinear diffusion model and an elastic-plastic constitutive model.[57,67] Specifically, the concentration of Li, c, is governed by the diffusion equation, $\partial c(r,t)/\partial t = \nabla \cdot [D(c,r)\nabla c(r,t)]$. Here the diffusivity D is a nonlinear function of c, given by $D = D_0[1/(1 - c) - 2\Omega c]$, where D_0 is the diffusivity constant, c is normalized by the Li concentration at the fully lithiated state, such that c varies between 0 and 1, and Ω determines the concentration profile around the reaction front. For numerical stability, the maximum of D is capped at $10^4 D_0$. In the finite element simulations, the Li concentrations behind the reaction front quickly reach the value of full lithiation (~1), whereas those ahead of the front remain zero. This creates a sharp reaction front which is consistent with experimental observations. It should be noted that there is a small Li concentration gradient behind the reaction front, such that Li can diffuse through the lithiated region continuously to reach the reaction front. To model the lithiation-induced deformation, an elastic and perfectly plastic model is used.[23,54] The total strain rate, $\dot{\varepsilon}_{ij}$, is a summation of three parts, $\dot{\varepsilon}_{ij} = \dot{\varepsilon}_{ij}^c + \dot{\varepsilon}_{ij}^e + \dot{\varepsilon}_{ij}^p$, where $\dot{\varepsilon}_{ij}^c$ is the chemical strain rate caused by lithiation and is proportional to the Li concentration rate $\dot{c}$, $\dot{\varepsilon}_{ij}^c = \beta_{ij}\dot{c}$, where β_{ij} is the lithiation expansion coefficient; $\dot{\varepsilon}_{ij}^e$ is the elastic strain rate and obeys Hooke's law according to $\dot{\varepsilon}_{ij}^e = [(1 + v)\dot{\sigma}_{ij} - v\dot{\sigma}_{kk}\delta_{ij}]/E$, where E is Young's modulus, v is Poisson's ratio, $\delta_{ij} = 1$ when $i = j$ and $\delta_{ij} = 0$ otherwise); the plastic strain rate, $\dot{\varepsilon}_{ij}^p$, obeys the classical J_2-flow rule and is given by $\dot{\varepsilon}_{ij}^p = \dot{\lambda}\sigma'_{ij}$, where $\dot{\lambda}$ is a scalar coefficient, and $\sigma'_{ij} = \sigma_{ij} - \sigma_{kk}\delta_{ij}/3$ is the deviatoric stress. In other words, plastic yielding occurs when the von Mises equivalent stress, $\sigma_{eq} = (3\sigma'_{ij}\sigma'_{ij}/2)^{1/2}$, equals the yield strength σ_Y.

ASSOCIATED CONTENT

Ⓢ Supporting Information

The Supporting Information is available free of charge on the ACS Publications website at DOI: 10.1021/acsnano.8b07319.

In situ SAED observation of lithiation of a single bare Bi_2S_3 NW (MPG)

In situ SAED observation of delithiation of a single bare Bi_2S_3 NW (MPG)

In situ TEM observation of lithiation of a single bare Bi_2S_3 NW (MPG)

In situ TEM observation of lithiation of a single core@shell Bi_2S_3@C NW (MPG)

In situ TEM observation of lithiation of a single yolk@shell Bi_2S_3@C NW (MPG)

In situ TEM observation of lithiation/delithiation cycling of a single bare Bi_2S_3 NW (MPG)

In situ TEM observation of lithiation/delithiation cycling of a single core@shell Bi_2S_3@C NW (MPG)

In situ TEM observation of lithiation/delithiation cycling of a single yolk@shell Bi_2S_3@C NW (MPG)

Simulation results of the lithiation evolution process of a core@shell NW (MPG)

Simulation results of the elastic-plastic deformation process of a core@shell NW (MPG)

Simulation results of the lithiation evolution process of a yolk@shell NW (MPG)

Simulation results of the elastic-plastic deformation process of a yolk@shell NW (MPG)

Schematic of fabrication process of yolk@shell Bi_2S_3@C NW, TEM images of bare Bi_2S_3 NW, Bi_2S_3@SiO_2 core@ shell NW and Bi_2S_3@SiO_2@C precursor core@shell@ shell NW. XRD patterns and TG result of bare Bi_2S_3 and yolk−shell@Bi_2S_3@C NW, GCD profiles of bare Bi_2S_3 and core@shell Bi_2S_3@C NW electrodes, *in situ* XRD and SAED results of bare Bi_2S_3@C NW electrodes during the second cycle, TEM images of bare Bi_2S_3 NW after delithiation, the equilibrium Li−S−Bi ternary phase diagram for Bi_2S_3, time-lapse TEM images of bare Bi_2S_3 NW at second lithiation, TEM images of bare Bi_2S_3 NW after lithiation, *in situ* TEM images of fast lithiation of core@shell Bi_2S_3@C NW, *in situ* TEM images of yolk@ shell Bi_2S_3@C NW under different lithiation/delithaiton cycles, comparison of ex-TEM images in the bare Bi_2S_3 NW, core@shell Bi_2S_3@C NWs and yolk@shell Bi_2S_3@ C NW electrode after long-term cycling and the computed energy barrier of Li migration, and the corresponding Li diffusion of bare Bi_2S_3 (PDF)

AUTHOR INFORMATION

Corresponding Authors
*E-mail: zhangqiaobao@xmu.edu.cn.
*E-mail: xzeng1@unl.edu.
*E-mail: mswang@xmu.edu.cn.

ORCID Ⓘ
Hong-Hui Wu: 0000-0002-1381-2281
Chenghao Yang: 0000-0002-3214-328X
Qiaobao Zhang: 0000-0002-3584-5201
Guiming Zhong: 0000-0003-2313-4741
Kai He: 0000-0003-4666-1800
Xiao Cheng Zeng: 0000-0003-4672-8585
Meilin Liu: 0000-0002-6188-2372
Ming-Sheng Wang: 0000-0003-3754-2850

Author Contributions
[#]These authors contributed equally to this work.

Notes
The authors declare no competing financial interest.

REFERENCES

(1) Zhu, C.; Usiskin, R. E.; Yu, Y.; Maier, J. The Nanoscale Circuitry of Battery Electrodes. *Science* 2017, *358*, eaao2808.

(2) Armand, M.; Tarascon, J.-M. Building Better Batteries. *Nature* 2008, *451*, 652−657.

(3) Li, M.; Lu, J.; Chen, Z.; Amine, K. 30 Years of Lithium-Ion Batteries. *Adv. Mater.* 2018, *30*, 1800561.

(4) Sun, Y.; Liu, N.; Cui, Y. Promises and Challenges of Nanomaterials for Lithium-Based Rechargeable Batteries. *Nat. Energy.* 2016, *1*, 16071.

(5) Choi, J. W.; Aurbach, D. Promise and Reality of Post-Lithium-Ion Batteries with High Energy Densities. *Nat. Rev. Mater.* **2016**, *1*, 16013.

(6) Mai, L.; Tian, X.; Xu, X.; Chang, L.; Xu, L. Nanowire Electrodes for Electrochemical Energy Storage Devices. *Chem. Rev.* **2014**, *114*, 11828−11862.

(7) Lu, J.; Chen, Z.; Ma, Z.; Pan, F.; Curtiss, L. A.; Amine, K. The Role of Nanotechnology in the Development of Battery Materials for Electric Vehicles. *Nat. Nanotechnol.* **2016**, *11*, 1031−1038.

(8) Ji, L.; Lin, Z.; Alcoutlabi, M.; Zhang, X. Recent Developments in Nanostructured Anode Materials for Rechargeable Lithium-Ion Batteries. *Energy Environ. Sci.* **2011**, *4*, 2682−2699.

(9) Ni, J.; Zhao, Y.; Liu, T.; Zheng, H.; Gao, L.; Yan, C.; Li, L. Strongly Coupled Bi_2S_3@CNT Hybrids for Robust Lithium Storage. *Adv. Energy Mater.* **2014**, *4*, 1400798.

(10) Ni, J.; Bi, X.; Jiang, Y.; Li, L.; Lu, J. Bismuth Chalcogenide Compounds Bi_2X_3 (X = O, S, Se): Applications in Electrochemical Energy Storage. *Nano Energy* **2017**, *34*, 356−366.

(11) Luo, W.; Li, F.; Li, Q.; Wang, X.; Yang, W.; Zhou, L.; Mai, L. Heterostructured Bi_2S_3-Bi_2O_3 Nanosheets with A Built-In Electric Field for Improved Sodium Storage. *ACS Appl. Mater. Interfaces* **2018**, *10*, 7201−7207.

(12) Wang, Z.; Li, Q.; Besenbacher, F.; Dong, M. Facile Synthesis of Single Crystal $PtSe_2$ Nanosheets for Nanoscale Electronics. *Adv. Mater.* **2016**, *28*, 10224−10229.

(13) Wang, Z.; Li, Q.; Xu, H.; Dahl-Petersen, C.; Yang, Q.; Cheng, D.; Cao, D.; Besenbacher, F.; Lauritsen, J. V.; Helveg, S.; Dong, M. Controllable Etching of MoS_2 Basal Planes for Enhanced Hydrogen Evolution through the Formation of Active Edge Sites. *Nano Energy* **2018**, *49*, 634−643.

(14) Wang, X.; Sun, F.; Yin, G.; Wang, Y.; Liu, B.; Dong, M. Tactile-Sensing Based on Flexible PVDF Nanofibers via Electrospinning: A Review. *Sensors* **2018**, *18*, 330.

(15) Zhong, Y.; Li, B.; Li, S.; Xu, S.; Pan, Z.; Huang, Q.; Xing, L.; Wang, C.; Li, W. Bi Nanoparticles Anchored in N-Doped Porous Carbon as Anode of High Energy Density Lithium Ion Battery. *Nano-Micro Lett.* **2018**, *10*, 56.

(16) Liang, H.; Ni, J.; Li, L. Bio-Inspired Engineering of Bi_2S_3 -PPy Yolk-Shell Composite for Highly Durable Lithium and Sodium Storage. *Nano Energy* **2017**, *33*, 213−220.

(17) Jung, H.; Park, C.-M.; Sohn, H.-J. Bismuth Sulfide and Its Carbon Nanocomposite for Rechargeable Lithium-Ion Batteries. *Electrochim. Acta* **2011**, *56*, 2135−2139.

(18) Liu, S.; Cai, Z.; Zhou, J.; Pan, A.; Liang, S. Chrysanthemum-Like Bi_2S_3 Nanostructures: A Promising Anode Material for Lithium-Ion Batteries and Sodium-Ion Batteries. *J. Alloys Compd.* **2017**, *715*, 432−437.

(19) Jin, R.; Li, G.; Zhang, Z.; Yang, L.-X.; Chen, G. Carbon Coated Flower Like Bi_2S_3 Grown on Nickel Foam as Binder-Free Electrodes for Electrochemical Hydrogen and Li-Ion Storage Capacities. *Electrochim. Acta* **2015**, *173*, 458−464.

(20) Zhao, Y.; Liu, T.; Xia, H.; Zhang, L.; Jiang, J.; Shen, M.; Ni, J.; Gao, L. Branch-Structured Bi_2S_3−CNT Hybrids with Improved Lithium Storage Capability. *J. Mater. Chem. A* **2014**, *2*, 13854−13858.

(21) Zhang, Y.; Fan, L.; Wang, P.; Yin, Y.; Zhang, X.; Zhang, N.; Sun, K. Coupled Flower-Like Bi_2S_3 and Graphene Aerogels for Superior Sodium Storage Performance. *Nanoscale* **2017**, *9*, 17694−17698.

(22) Li, Y.; Lu, J.; Cheng, X.; Shi, H.; Zhang, Y. Interfacial Lithiation Induced Leapfrog Phase Transformation in Carbon Coated Se Cathode Observed by *In-Situ* TEM. *Nano Energy* **2018**, *48*, 441−447.

(23) Zhang, L. Q.; Liu, X. H.; Liu, Y.; Huang, S.; Zhu, T.; Gui, L.; Mao, S. X.; Ye, Z. Z.; Wang, C. M.; Sullivan, J. P.; Huang, J. Y. Controlling the Lithiation-Induced Strain and Charging Rate in Nanowire Electrodes by Coating. *ACS Nano* **2011**, *5*, 4800−4809.

(24) Liu, J.; Kopold, P.; Wu, C.; van Aken, P. A.; Maier, J.; Yu, Y. Uniform Yolk−Shell Sn_4P_3@C Nanospheres as High-Capacity and Cycle-Stable Anode Materials for Sodium-Ion Batteries. *Energy Environ. Sci.* **2015**, *8*, 3531−3538.

(25) Chen, J.; Fan, X.; Ji, X.; Gao, T.; Hou, S.; Zhou, X.; Wang, L.; Wang, F.; Yang, C.; Chen, L.; Wang, C. Intercalation of Bi Nanoparticles into Graphite Results in An Ultra-Fast and Ultra-Stable Anode Material for Sodium-Ion Batteries. *Energy Environ. Sci.* **2018**, *11*, 1218−1225.

(26) Song, J.; Yan, P.; Luo, L.; Qi, X.; Rong, X.; Zheng, J.; Xiao, B.; Feng, S.; Wang, C.; Hu, Y.-S.; Lin, Y.; Sprenkle, V. L.; Li, X. Yolk-Shell Structured Sb@C Anodes for High Energy Na-Ion Batteries. *Nano Energy* **2017**, *40*, 504−511.

(27) Cao, K.; Li, P.; Zhang, Y.; Chen, T.; Wang, X.; Zhang, S.; Liu, J.; Wang, H. *In Situ* Tem Investigation on Ultrafast Reversible Lithiation and Delithiation Cycling of Sn@C Yolk-Shell Nanoparticles as Anodes for Lithium Ion Batteries. *Nano Energy* **2017**, *40*, 187−194.

(28) Zhang, H.; Zhou, L.; Noonan, O.; Martin, D. J.; Whittaker, A. K.; Yu, C. Tailoring the Void Size of Iron Oxide@Carbon Yolk-Shell Structure for Optimized Lithium Storage. *Adv. Funct. Mater.* **2014**, *24*, 4337−4342.

(29) Xie, D.; Xia, X.; Zhong, Y.; Wang, Y.; Wang, D.; Wang, X.; Tu, J. Exploring Advanced Sandwiched Arrays by Vertical Graphene and N-Doped Carbon for Enhanced Sodium Storage. *Adv. Energy Mater.* **2017**, *7*, 1601804.

(30) Mo, R.; Rooney, D.; Sun, K.; Yang, H. Y. 3D Nitrogen-Doped Graphene Foam with Encapsulated Germanium/Nitrogen-Doped Graphene Yolk-Shell Nanoarchitecture for High-Performance Flexible Li-Ion Battery. *Nat. Commun.* **2017**, *8*, 13949.

(31) Wood, K. N.; O'Hayre, R.; Pylypenko, S. Recent Progress on Nitrogen/Carbon Structures Designed for Use in Energy and Sustainability Applications. *Energy Environ. Sci.* **2014**, *7*, 1212−1249.

(32) Zhang, Q.; Chen, H.; Luo, L.; Zhao, B.; Luo, H.; Han, X.; Wang, J.; Wang, C.; Yang, Y.; Zhu, T.; Liu, M. Harnessing the Concurrent Reaction Dynamics in Active Si and Ge to Achieve High Performance Lithium-Ion Batteries. *Energy Environ. Sci.* **2018**, *11*, 669−681.

(33) Wu, C.; Maier, J.; Yu, Y. Generalizable Synthesis of Metal-Sulfides/Carbon Hybrids with Multiscale, Hierarchically Ordered Structures as Advanced Electrodes for Lithium Storage. *Adv. Mater.* **2016**, *28*, 174−180.

(34) Xu, X.; Liu, W.; Kim, Y.; Cho, J. Nanostructured Transition Metal Sulfides for Lithium Ion Batteries: Progress and challenges. *Nano Today* **2014**, *9*, 604−630.

(35) Liu, J.; Wu, C.; Xiao, D.; Kopold, P.; Gu, L.; van Aken, P. A.; Maier, J.; Yu, Y. MOF-Derived Hollow Co_9S_8 Nanoparticles Embedded in Graphitic Carbon Nanocages with Superior Li-Ion Storage. *Small* **2016**, *12*, 2354−2364.

(36) Zhang, Q.; Wang, J.; Dong, J.; Ding, F.; Li, X.; Zhang, B.; Yang, S.; Zhang, K. Facile General Strategy toward Hierarchical Mesoporous Transition Metal Oxides Arrays on Three-Dimensional Macroporous Foam with Superior Lithium Storage Properties. *Nano Energy* **2015**, *13*, 77−91.

(37) Zheng, Z.; Zao, Y.; Zhang, Q.; Cheng, Y.; Chen, H.; Zhang, K.; Wang, M.-S.; Peng, D.-L. Robust Erythrocyte-Like Fe_2O_3@Carbon with Yolk-Shell Structures as High-Performance Anode for Lithium Ion Batteries. *Chem. Eng. J.* **2018**, *347*, 563−573.

(38) Ou, X.; Yang, C.; Xiong, X.; Zheng, F.; Pan, Q.; Jin, C.; Liu, M.; Huang, K. A New rGO-Overcoated Sb_2Se_3 Nanorods Anode for Na^+ Battery: *In Situ* X-Ray Diffraction Study on A Live Sodiation/Desodiation Process. *Adv. Funct. Mater.* **2017**, *27*, 1606242.

(39) Yin, K.; Zhang, M.; Hood, Z. D.; Pan, J.; Meng, Y. S.; Chi, M. Self-Assembled Framework Formed During Lithiation of SnS_2 Nanoplates Revealed by *In Situ* Electron Microscopy. *Acc. Chem. Res.* **2017**, *50*, 1513−1520.

(40) Stephenson, T.; Li, Z.; Olsen, B.; Mitlin, D. Lithium Ion Battery Applications of Molybdenum Disulfide (MoS_2) Nanocomposites. *Energy Environ. Sci.* **2014**, *7*, 209−231.

(41) Shi, S.; Gao, J.; Liu, Y.; Zhao, Y.; Wu, Q.; Ju, W.; Ouyang, C.; Xiao, R. Multi-Scale Computation Methods: Their Applications in Lithium-Ion Battery Research and Development. *Chin. Phys. B* **2016**, *25*, 018212.

(42) Shi, J.; Wang, Z.; Fu, Y. Q. Density Functional Theory Study of Lithium Diffusion at the Interface Between Olivine-Type LiFePO₄ and LiMnPO₄. *J. Phys. D: Appl. Phys.* **2016**, *49*, 505601.

(43) Zheng, Y.; Zhou, T.; Zhao, X.; Pang, W. K.; Gao, H.; Li, S.; Zhou, Z.; Liu, H.; Guo, Z. Atomic Interface Engineering and Electric-Field Effect in Ultrathin Bi₂MoO₆ Nanosheets for Superior Lithium Ion Storage. *Adv. Mater.* **2017**, *29*, 1700396.

(44) Van der Ven, A.; Ceder, G.; Asta, M.; Tepesch, P. First-Principles Theory of Ionic Diffusion with Nondilute Carriers. *Phys. Rev. B: Condens. Matter Mater. Phys.* **2001**, *64*, 184307.

(45) Huang, H.; Wu, H.-H.; Wang, X.; Huang, B.; Zhang, T. Enhancing Sodium Ionic Conductivity in Tetragonal-Na₃PS₄ by Halogen Doping: A First Principle Investigation. *Phys. Chem. Chem. Phys.* **2018**, *20*, 20525−20533.

(46) Liu, X. H.; Huang, J. Y. *In Situ* TEM Electrochemistry of Anode Materials in Lithium Ion Batteries. *Energy Environ. Sci.* **2011**, *4*, 3844−3860.

(47) Liu, X. H.; Liu, Y.; Kushima, A.; Zhang, S.; Zhu, T.; Li, J.; Huang, J. Y. *In Situ* TEM Experiments of Electrochemical Lithiation and Delithiation of Individual Nanostructures. *Adv. Energy Mater.* **2012**, *2*, 722−741.

(48) Li, X.; Zhao, L.; Li, P.; Zhang, Q.; Wang, M.-S. *In-Situ* Electron Microscopy Observation of Electrochemical Sodium Plating and Stripping Dynamics on Carbon Nanofiber Current Collectors. *Nano Energy* **2017**, *42*, 122−128.

(49) Huang, J. Y.; Zhong, L.; Wang, C. M.; Sullivan, J. P.; Xu, W.; Zhang, L. Q.; Mao, S. X.; Hudak, N. S.; Liu, X. H.; Subramanian, A.; Fan, H.; Qi, L.; Kushima, A.; Li, J. *In Situ* Observation of the Electrochemical Lithiation of A Single SnO₂ Nanowire Electrode. *Science* **2010**, *330*, 1515−1520.

(50) Kushima, A.; Liu, X. H.; Zhu, G.; Wang, Z. L.; Huang, J. Y.; Li, J. Leapfrog Cracking and Nanoamorphization of ZnO Nanowires during *In Situ* Electrochemical Lithiation. *Nano Lett.* **2011**, *11*, 4535−4541.

(51) Gregorczyk, K. E.; Liu, Y.; Sullivan, J. P.; Rubloff, G. *In Situ* Transmission Electron Microscopy Study of Electrochemical Lithiation and Delithiation Cycling of the Conversion Anode RuO2. *ACS Nano* **2013**, *7*, 6354−6360.

(52) Wang, X.; Tang, D. M.; Li, H.; Yi, W.; Zhai, T.; Bando, Y.; Golberg, D. Revealing the Conversion Mechanism of CuO Nanowires during Lithiation-Delithiation by *In Situ* Transmission Electron Microscopy. *Chem. Commun.* **2012**, *48*, 4812−4814.

(53) Su, Q.; Du, G.; Zhang, J.; Zhong, Y.; Xu, B.; Yang, Y.; Neupane, S.; Kadel, K.; Li, W. *In Situ* Transmission Electron Microscopy Investigation of the Electrochemical Lithiation-Delithiation of Individual Co₉S₈/Co-Filled Carbon Nanotubes. *ACS Nano* **2013**, *7*, 11379−11387.

(54) Zhao, K.; Pharr, M.; Vlassak, J. J.; Suo, Z. Inelastic Hosts as Electrodes for High-Capacity Lithium-Ion Batteries. *J. Appl. Phys.* **2011**, *109*, 016110.

(55) Huang, S.; Fan, F.; Li, J.; Zhang, S.; Zhu, T. Stress Generation during Lithiation of High-Capacity Electrode Particles in Lithium Ion Batteries. *Acta Mater.* **2013**, *61*, 4354−4364.

(56) Yang, H.; Fan, F.; Liang, W.; Guo, X.; Zhu, T.; Zhang, S. A Chemo-Mechanical Model of Lithiation in Silicon. *J. Mech. Phys. Solids* **2014**, *70*, 349−361.

(57) Wang, J. W.; He, Y.; Fan, F.; Liu, X. H.; Xia, S.; Liu, Y.; Harris, C. T.; Li, H.; Huang, J. Y.; Mao, S. X.; Zhu, T. Two-Phase Electrochemical Lithiation in Amorphous Silicon. *Nano Lett.* **2013**, *13*, 709−715.

(58) Liu, X. H.; Zheng, H.; Zhong, L.; Huang, S.; Karki, K.; Zhang, L. Q.; Liu, Y.; Kushima, A.; Liang, W. T.; Wang, J. W.; et al. Anisotropic Swelling and Fracture of Silicon Nanowires during Lithiation. *Nano Lett.* **2011**, *11*, 3312−3318.

(59) Liu, J.; Li, N.; Goodman, M. D.; Zhang, H. G.; Epstein, E. S.; Huang, B.; Pan, Z.; Kim, J.; Choi, J. H.; Huang, X.; et al. Mechanically and Chemically Robust Sandwich-Structured C@Si@ C Nanotube Array Li-Ion Battery Anodes. *ACS Nano* **2015**, *9*, 1985−1994.

(60) Hutchinson, J.; Neale, K. In Finite Strain *J₂* Deformation Theory. *Proceedings of the IUTAM Symposium on Finite Elasticity*; Springer: Dordrecht, The Netherlands, 1981; pp 237−247.

(61) Pei, F.; An, T.; Zang, J.; Zhao, X.; Fang, X.; Zheng, M.; Dong, Q.; Zheng, N. From Hollow Carbon Spheres to N-Doped Hollow Porous Carbon Bowls: Rational Design of Hollow Carbon Host for Li-S Batteries. *Adv. Energy Mater.* **2016**, *6*, 1502539.

(62) Kresse, G.; Furthmüller, J. Efficient Iterative Schemes for Ab Initio Total-Energy Calculations Using A Plane-Wave Basis Set. *Phys. Rev. B: Condens. Matter Mater. Phys.* **1996**, *54*, 11169.

(63) Hutter, J.; Iannuzzi, M.; Schiffmann, F.; VandeVondele, J. CP2K: Atomistic Simulations of Condensed Matter Systems. *Wiley Interdiscip. Rev. Comput. Mol. Sci.* **2014**, *4*, 15−25.

(64) Sheppard, D.; Xiao, P.; Chemelewski, W.; Johnson, D. D.; Henkelman, G. A Generalized Solid-State Nudged Elastic Band Method. *J. Chem. Phys.* **2012**, *136*, 074103.

(65) Jain, A.; Ong, S. P.; Hautier, G.; Chen, W.; Richards, W. D.; Dacek, S.; Cholia, S.; Gunter, D.; Skinner, D.; Ceder, G.; Persson, K. A. Commentary: The Materials Project: A Materials Genome Approach to Accelerating Materials Innovation. *APL Mater.* **2013**, *1*, 011002.

(66) Ong, S. P.; Richards, W. D.; Jain, A.; Hautier, G.; Kocher, M.; Cholia, S.; Gunter, D.; Chevrier, V. L.; Persson, K. A.; Ceder, G. Python Materials Genomics (PYMATGEN): A Robust, Open-Source Python Library for Materials Analysis. *Comput. Mater. Sci.* **2013**, *68*, 314−319.

(67) Zhang, S.; Zhao, K.; Zhu, T.; Li, J. Electrochemomechanical Degradation of High-Capacity Battery Electrode Materials. *Prog. Mater. Sci.* **2017**, *89*, 479−521.